Biosensors and Bioelectronics 126 (2019) 455–462

Contents lists available at ScienceDirect

Biosensors and Bioelectronics

journal homepage: www.elsevier.com/locate/bios

Ultrasensitive label- and amplification-free photoelectric protocols based on sandwiched layer-by-layer plasmonic nanocomposite films for the detection of alpha-fetoprotein

Wen-Yin Ko[a], Tzu-Jung Tien[a], Chuen-Yuan Hsu[b], Kuan-Jiuh Lin[a,*]

[a] Department of Chemistry and Research Center for Sustainable Energy and Nanotechnology, National Chung Hsing University, Taichung 402, Taiwan
[b] IVD Dept. Siward Crystal Technology Co., Ltd., Taiwan

ARTICLE INFO

Keywords:
Immunosensor
Label- and amplification-free
Photoelectric effect
Au/TiO_2
Layer-by-layer
Sandwich

ABSTRACT

A label- and amplification-free photoelectric immunosensor based on well-defined layer-by-layer sandwich-structured AuNP/TNW/AuNP composite is proposed for direct and ultrasensitive detection of α-fetoprotein (AFP). The AuNP/TNW/AuNP composite is produced by assembling an Au nanoparticle underlayer and anatase TiO_2 nanowires (TNW) onto the FTO substrate, followed by decorating Au nanoparticles onto the TNW surface, through a simple sputtering and hydrothermal process. The resulting AuNP/TNW/AuNP electrode exhibits a 14-fold and 2-fold enhancement in photocurrent density under simulated sunlight compared with that of bare TNW and AuNP/TNW, respectively, which benefits from the SPR-induced photoabsorption increment and charge separation improvement in Au nanoparticle and interfacial charge transfer promotion at the TiO_2/substrate interface in the Au underlayer. As a proof of concept, the AFP antigen can be quantitatively detected by the proposed AuNP/TNW/AuNP coupled with anti-AFP through the analysis of the photocurrent change. This novel AFP photoelectric immunosensor exhibited sensitive detection of AFP with an ultrahigh sensitivity of 0.001 ng mL^{-1} and good specific selectivity. Moreover, the practical determination of AFP in human serum is also investigated, demonstrating its applicability and potential attraction for clinical tests and disease diagnosis.

1. Introduction

Early-stage diagnosis for cancers and other diseases relies largely on the detection of biomarkers with a quick, sensitive, and accurate analysis. In recent decades, many efforts have been devoted to the exploration of more effective approaches, simpler detection processes, and enhanced detection sensitivity. A simple label-free biosensing platform of plasmonic optical-immunosensors based on glass-based Au-LSPR biochips assembled by mono-layered Au nanoparticles and embedded on transparent glass substrates has been developed previously in our lab (Hsu et al., 2011). However, the detection limit was only at the microgram level for the target molecules directly captured by Au nanoparticles. To further enhance sensitivity, a gold cluster (less than 50 nm in size) as an amplification reagent was introduced into the glass-based Au-LSPR biochips by a drop-by-drop process after the glass-based Au-LSPR biochips were coupled with antibody and target antigen, where the gold cluster would attach onto the surface of the target antigen (unpublished work, see Fig. S1). With the plasmonic coupling from the gold cluster, the detection limits can yield a 1000-fold increase in sensitivity compared to the one without gold cluster. The glass-based Au-LSPR biochips with Au-cluster amplification reagent has been recently launched commercially for use in cTnI detection, improving the detection limit down to 80 pg mL^{-1} (unpublished work, see Fig. S1). However, the complex amplification strategy, time-consuming detection process (30 min to accomplish the detection), extra reagent cost, and assay time can hinder its further development. Therefore, the development of a label- and amplification-free biosensor for highly sensitive detection is desirable.

Photoelectric biosensing, through the usage of light and electrical energy on photoactive electrodes for sensor excitation and determination, has been demonstrated to minimize the background noise and increase sensitivity compared with the optical LSPR-based biosensors. It has been widely used in biological analyses owing to its desirable advantages of remarkable sensitivity, time-saving experimental process, low-cost, ease of integration, and simple instrumentation (Chen et al., 2018a; Haddour et al., 2006). The basic photoelectric process refers to photon-electricity conversion, in which the photocurrent signal would generate as the photon and electron transfer between the electrode,

* Corresponding author.
E-mail address: kjlin@dragon.nchu.edu.tw (K.-J. Lin).

https://doi.org/10.1016/j.bios.2018.11.020
Received 14 August 2018; Received in revised form 14 November 2018; Accepted 14 November 2018
Available online 19 November 2018
0956-5663/

photoactive materials, and electrolyte (Devadoss et al., 2015; Li et al., 2016). Therefore, the development of photoactive electrodes with high photoelectric effect, which can efficiently convert the photoirradiation into an electrical signal in order to enhance analytical performances of the photoelectric biosensors, has great significance in meeting sensing demands. The anatase TiO_2, emerged as an exceptional photoactive material, has been intensively studied in biosensing applications because of its non-toxicity, environmental safety, hydrophilicity, low cost, bio-compatibility, and stability against photocorrosion (Bai and Zhou, 2014; Gao et al., 2015; Guo et al., 2017b; Yang et al., 2015a). In particular for photoelectric biosensors, there has been increased focus on the development of TiO_2-based photoactive materials for label- and amplification-free photoelectric detection, which require simpler instruments and are easier to miniaturize than conventional label-free optical methods. For example, Ochratoxin A detection based on CdSe nanoparticles sensitized anatase TiO_2-functionalized electrodes (Yang et al., 2015a). Sensitive detection of OTA has been accomplished using TiO_2/S-$BiVO_4$@Ag_2S nanocomposites (Feng et al., 2018). Carcinoembryonic antigen detection based on 2D TiO_2 nanosheets and carboxylated graphitic carbon has also been reported (Wang et al., 2016). Furthermore, glutathione detection by IrO_2–Hemin–TiO_2 nanowire (IrO_2–Hemin–TNW) arrays (Tang et al., 2013) and DNA sensor based on TiO_2 electrodes (Lu et al., 2006) has been demonstrated. Finally, mercury(II) ions can be detected in human serum through Au@Ag nanorods modified with TiO_2 nanosheets (Zhang et al., 2016), and Hg^{2+} can be detected through the quenching of photogenerated electrons based on N-doped TiO_2 (Han et al., 2015). However, these abovementioned sensing methods always required complicated and time-consuming processes, which hindered their wide and actual applications. Therefore, the development of a simple method to fabricate TiO_2-based photoactive electrodes for constructing a label- and amplification-free photoelectric sensor is necessary.

We previously achieved an antireflective property-based photoelectrode assembled by anatase TNWs with a high-porosity cross-linked geometry through a one-step alkaline hydrothermal process (Chen et al., 2012), which could potentially reduce the reflection of incident light as well as increase the device performances for photoelectric detection. Nevertheless, its drawbacks including a narrow visible light response range (~ 3.2 eV), low separation efficiency of photoinduced electron-hole pairs, and high interfacial charge-transfer resistance at the interface between electrode, electrolyte, and selected substrate limited its application as an efficient photoactive electrode of photoelectric biosensors (Chen et al., 2013; Wang et al., 2018; Yang et al., 2015b). Integration of Au nanoparticles with TiO_2 brings drastic interest for improving the photoelectric effect, owing to the localized surface plasmon resonance (LSPR) effect of introduced Au nanoparticles giving rise to enhanced light harvesting and reduced photo-excited electron-hole recombination (Bora et al., 2016; Chen et al., 2018b; Liu et al., 2018; Pu et al., 2013; Wang et al., 2013; Yen et al., 2017; Zhang et al., 2013). Based on the plasmonic energy-transfer enhancement, the conjugation of immunoassay with Au/TiO_2 photoactive electrode for detecting the antibody-antigen binding seems to be a promising technique for bioanalysis. Among the few examples of photoelectrochemical immunosensors based on Au-TiO_2 composites available in the literature (Guo et al., 2017a; Liu et al., 2018), the most important one is related to the Au-doped TiO_2 nanotube arrays on Ti foils, where enhanced photocurrent sensitivity for the detection of α-synuclein at the applied potential of 0.6 V was achieved by introducing the {Ab_2-Au-GOx} bioconjugates as the signal amplifier, which contained a secondary antibody (Ab_2) and glucose oxidase (GO_x) label linked to Au nanoparticles (An et al., 2010). However, this method involved a complicated procedure, expensive labels, and signal amplifiers, thereby hindering its applications. Thus, the design of a label-free immunosensor employing a Au/TiO_2 nanocomposite as a photoactive-sensor electrode without using any amplification reagent for the determination of proteins in photoelectric bioanalysis still remains a challenge.

In this study, a novel label- and amplification-free photoelectric protocol based on well-defined layer-by layer sandwich-type AuNP/TNW/AuNP ultra-thin film was successfully fabricated on FTO substrates for sensitive detection of cancer biomarker α-fetoprotein (AFP). The AuNP/TNW/AuNP composite on FTO was synthesized by firstly growing the antireflective one-dimensional anatase-type TNW on Au/FTO substrate, which was pre-sputtered with an Au nanoparticle underlayer (called the Au underlayer) onto the FTO surface, by an alkaline hydrothermal process, followed by sputtering of Au nanoparticles with an average size of 9.3 ± 2.59 nm onto the TNW surface. A prominent enhancement in photocurrent of the AuNP/TNW/AuNP composite compared to AuNP/TNW and TNW electrodes was attained, which could be ascribed to the injection of enhanced photo-absorption and photo-excited electrons from the Au nanoparticle induced by the SPR enhancement as well as the increased vectorial transfer of the photogenerated charge carrier at the TiO_2/substrate interface induced by Au underlayer. The fabricated photoelectric immunosensor of sandwich-type AuNP/TNW/AuNP electrode for AFP detection exhibited a high sensitivity and good selectivity. Moreover, good performance in real human serum was also achieved, indicating its great potential in the practical determination of AFP for clinical tests and disease diagnosis.

2. Experimental section

2.1. Materials

FTO glass with a thickness of 2.2 mm (1.5 cm × 3 cm, TEC-7; Hartford, CT, USA) was used as the substrate for the growth of AuNP/TNW/AuNP. Sodium hydroxide (NaOH) (> 98%), nitric acid (HNO_3) (65%), and potassium chloride (KCl) were obtained from Merck. Human alpha-fetoprotein (AFP) (native protein, human cord serum, MBS537909) and anti-AFP antibody (monoclonal, MBS530361) were purchased from MyBioSource. Human serum was purchased from Merck Millipore (S1–100 mL). Phosphate buffered saline (10 × Solution, UR-PBS001), potassium hexacyanoferrate(II) ($K_4[Fe(CN)_6]\cdot 3H_2O$) (98%), and potassium hexacyanoferrate(III) ($K_4[Fe\{CN\}_6]$) (98%) were from UniRegion Bio-Tech, Taiwan, VETEC, and JANSSEN, respectively. All of the chemicals were used as received without any purification. Milli-Q water (18 MΩ resistivity; Millipore System) was used for all experiments.

2.2. Apparatus

Scanning electron microscopy (SEM) was performed with a Zeiss Ultra-Plus field emission scanning electron microscope (FESEM) with an accelerating voltage of 3 kV. The morphology, crystallinity, and element mapping of the products were also characterized by a JEM 2010 high-resolution transmission electron microscope (HRTEM) and a spherical aberration corrected scanning transmission electron microscope (Cs-corrected STEM), operating at accelerating voltages of 200 kV. The samples for TEM investigation were prepared by both a conventional method and FIB milling. The optical absorption properties were studied by recording the UV–visible absorption spectra with a UV/vis/NIR spectrometer (Lambda 900, Perkin-Elmer). The Raman analysis was performed via the Raman microspectroscopy system of Nanofinder 30 (Tokyo Instruments, Inc.) with a He–Ne laser (λex = 632.8 nm) and a semiconductor laser (λex = 488 nm) as the excitation sources. All of the photoeletrochemical measurements and the electrochemical impedance spectroscopy (EIS) measurements were carried out on a PARSTAT 2263 advanced electrochemical system under illumination by Newport solar simulator with AM 1.5G (100 mW/cm^2).

2.3. Synthesis of AuNP/TNW/AuNP composites

The AuNP/TNW/AuNP composites were prepared by following the synthetic procedure we previously reported with a slight modification

(Yen et al., 2015). Briefly, the anatase TNW was first grown via an alkaline hydrothermal treatment on a FTO with pre-sputtered Au film of 1 nm in thickness as the Au underlayer and subsequent Ti film of 50 nm in thickness with 5 M NaOH aqueous solution at 80 °C for 1.5 h. The Ti film was sputtered through a magnetic sputter instrument (TVC-M8C8TV, Transvac co. Ltd.) equipped with a Ti target at a sputter rate of 4 nm/s with an Ar gas flow rate of 300 sccm and a sputtering pressure of 1.2×10^{-3} Torr, in which the distance between the sputtering target and substrate was 90 cm. Subsequently, the Au layer with a thickness of 0.8 nm was deposited onto the TNW surface by using the sputtering method for the growth of Au nanoparticle, where the TNW was used as the skeleton for the Au-sputtered coating (Fig. S2), similar to the results presented in our previous work (Yen et al., 2015). The gold films were sputtered under Ar gas at a sputter rate of 90 mm/s with 0.35 kW for the growth of the Au underlayer, and 0.30 kW for the growth of Au nanoparticle. Finally, the film was annealed at 500 °C for 1 h to obtain the AuNP/TNW/AuNP composites on FTO.

2.4. Construction of the photoelectric immunosensor

The anti-AFP antibody was firstly diluted to 2 ppm with PBS and stored at −20 °C. Next, the prepared AuNP/TNW/AuNP electrode was immersed in the anti-AFP antibody PBS (30 μL) for 1.5 h to allow for the formation of non-covalent conjugations between the anti-AFP antibody and AuNP surface via hydrophobic and ionic interactions (Jazayeri et al., 2016). Then, the electrode was rinsed with PBS solution and Milli-Q water, followed by drying at room temperature under a stream of N_2 gas. Finally, the electrode was immersed in AFP (in PBS) at different concentrations for 1.5 h at room temperature. After washing with PBS and drying in a N_2 stream, the electrode was used as the photoelectric immunosensor for AFP detection.

2.5. Analysis of AFP

The analysis was performed in a three-electrode system, with an Ag/AgCl (saturated with KCl) as the reference electrode, Pt wire as the counter electrode, and the prepared electrode as the working electrode in PBS (pH 7.4) under simulated sunlight coupled with an AM 1.5G filter and the illumination direction of the solar simulator is perpendicular to the electrode surface. The scheme of processes for the fabrication construction of photoelectric AFP immunosensor was shown in Fig. S3.

2.6. Detection of AFP in human serum

The human serum was diluted 100 times with 10 mM PBS (pH 7.4) and stored at −20 °C for AFP detection. The practical application experiment was performed by spiking of human serum with target AFP of 0.05, 0.1, 0.5, or 1 ng/mL and analyzed by the proposed sandwich-structured AuNP/TNW/AuNP photoelectric immunosensor. For each sample, three independent tests were undertaken and the corresponding concentration were calculated according to the calibration curve in Fig. 6(a).

3. Results and discussions

3.1. Synthesis and characterization of AuNP/TNW/AuNP

Structural characterization was performed by SEM in cross-sections and top-views to study surface and lateral morphologies of the prepared AuNP/TNW/AuNP composites, as shown in Fig. 1(a) and (b). It could be observed that exclusively homogenous and large amounts of AuNP/TNW as well as a highly porous framework were deposited onto the surface of FTO with pre-deposited Au nanoparticles as the underlayer (Au/FTO) to achieve layer-by-layer sandwich-structured AuNP/TNW/AuNP composite films with a thickness of ~254.5 nm on the FTO substrate. The TNWs, formed from the Ti wet corrosion reaction in alkaline solution, were found to grow vertically on the Au/FTO substrate and bent on top. The TNWs kept a nearly vertical growth oriented from the substrate could be ascribed to the downward growth of titanate nanowires as the Ti corrosion region grew downward (Dong et al., 2007). It showed that the near-spherical Au nanoparticles with an average size of 9.3 ± 2.59 nm were uniformly deposited along the surface of TNW with an average diameter of 11.4 ± 2.40 nm. According to our previous study (Chen et al., 2012), the highly porous TNW structure could provide light trapping benefits because of its outstanding antireflection property. The EDX data shown in Fig. 1(c) indicated the detection of Ti, O, and Au signals from the AuNP/TNW/AuNP thin film, suggesting that the composite was comprised of TiO_2 and Au. Fig. 1(d) shows the Raman spectra of prepared TNW and AuNP/TNW/AuNP samples. The observed Raman bands were approximately at 141.9, 395.7, 514.2, and 636.3 cm^{-1}, and can be assigned to the E_g, B_{1g}, A_{1g}, and E_g mode of the anatase TiO_2, respectively, which were consistent with the result obtained from the HRTEM data. Importantly, the crystalline of the characteristic E_g peak at 141.9 cm^{-1} shifts to a higher wavenumber by ~4.6 cm^{-1} (inset of Fig. 1d) after the decoration of Au nanoparticles with TNW, demonstrating the increased crystalline defects within the TiO_2 and the interaction between Au and TiO_2 (Zhao et al., 2016).

To further investigate the structures of the synthesized composite, the AuNP/TNW/AuNP sample was subjected to TEM and elemental mappings, as shown in Fig. 2. Fig. 2(a) shows a cross-sectional TEM image of the AuNP/TNW/AuNP composites, where the corresponding TEM sample was prepared by site-specific FIB milling. A sandwich-like architecture composed of a nanoparticle-nanowire-nanoparticle structure was obtained, in which numerous TNWs interweaved into a porous morphology and decorated with spherical-like Au nanoparticles were found to deposit onto the surface of the Au nanoparticle-coated FTO substrate. The elemental mapping result shown in Fig. 2(b) further demonstrated the formation of AuNP/TNW/AuNP composites onto the FTO, in which a trace of elemental Au was introduced to the surface of the FTO and TNW with a homogeneous distribution of elemental Ti and O. The HRTEM image captured from the AuNP/TNW/AuNP sample clearly exhibited the single-crystalline nature of both TiO_2 NWs and Au nanoparticles (Fig. 2c). Two completely different lattice fringes were revealed, in which the interplanar spacing of 0.352 nm was assigned to the (101) plane in anatase TiO_2, and another lattice spacing of 0.235 nm corresponds to the (111) plane of Au nanoparticles, respectively, revealing that the Au nanoparticles were attached on the anatase-TNW surface (Yu et al., 2017; Zhang et al., 2015).

The interaction between Au nanoparticles and TNW was further demonstrated with UV–visible absorption spectroscopy. As shown in Fig. 3(a), the AuNP/TNW/AuNP composite exhibited an absorbance band at approximately 565.8 nm, which was ascribed to the typical characteristic of the LSPR band of Au nanoparticles. It was noted that the LSPR band was observed to red shift by ~46 nm compared to that of the citrate-stabilized Au nanoparticles with similar particle size dip-coated onto ITO substrates (~520 nm). The observed remarkable red shift could be attributed to the change in refractive index of the surrounding environment of Au nanoparticles resulting from the particle–oxide interfacial interactions, according to the equation $\lambda_{sp} = 2\pi c(\varepsilon_0 m_e[\varepsilon_\infty + k n_m^2]/Ne^2)^{1/2}$, where κ is the nanoparticle geometry-dependent factor (e.g., $\kappa = 2$ for a sphere), N is the electron density of the metal, ε_0 is the permittivity of free space, ε_∞ is the high-frequency contribution to the dielectric function, n_m is the medium refractive index (RI), and m_e is the effective electron mass (Atwater and Polman, 2010; Yen et al., 2015). This result demonstrates the strong interaction between Au nanoparticles and the TNW, where coupling between Au nanoparticles and TiO_2 has been shown to improve plasmon-induced charge transportation, enabling the SPR-enhanced photocurrent property. The onset of the absorbance edge for the TNW sample was clearly under 400 nm because of the wide band gap of around 3.2 eV. The

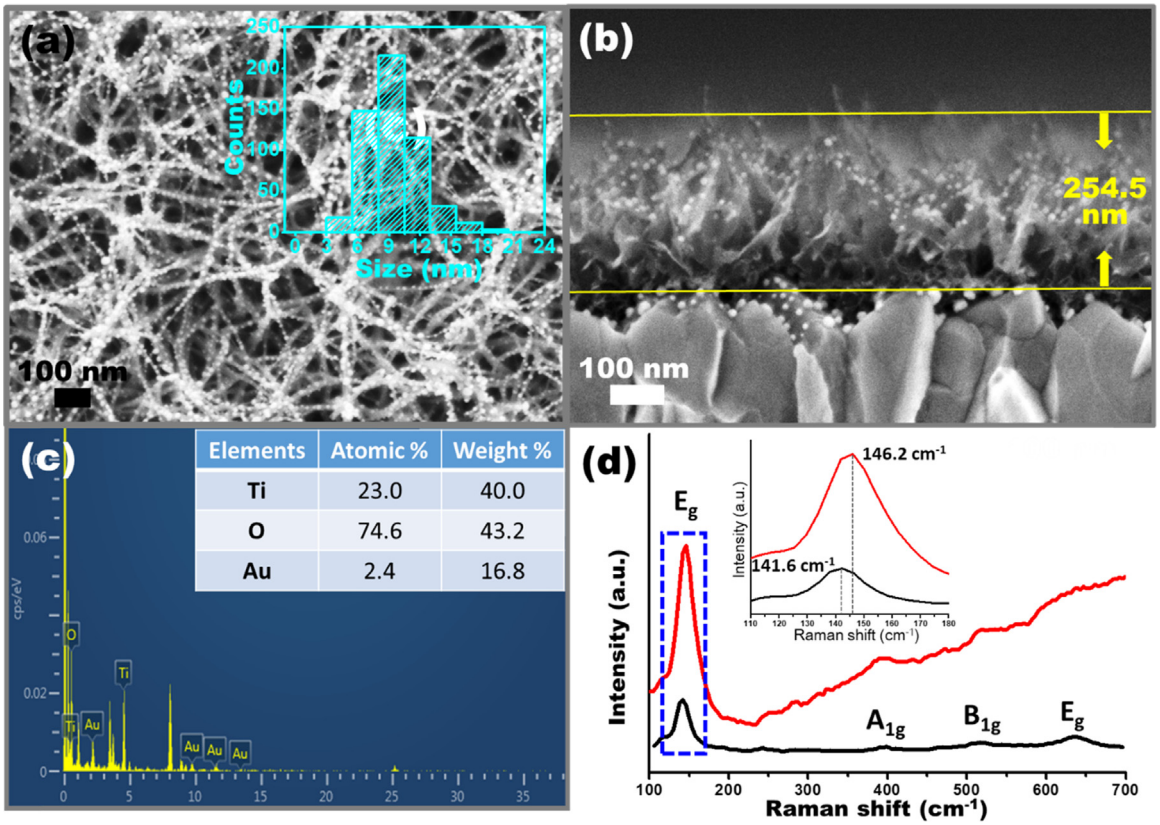

Fig. 1. Scanning electron microscopy images of (a) top-view and (b) cross-section of the prepared AuNP/TNW/AuNP composites on FTO substrate. Size distribution of the Au nanoparticles along the surface of the TiO_2 nanowires (TNWs) is shown in the inset of Figure (a). (c) The corresponding EDX measurement. (d) Raman spectra of the TNW sample (black curve) and AuNP/TNW/AuNP composites (red curve). (For interpretation of the references to color in this figure legend, the reader is referred to the web version of this article).

characteristic LSPR band in the range of 400–700 nm after the decoration of Au nanoparticles shifted the absorption edge to the visible light region, resulting in enhanced light harvesting. The enhanced light absorption can therefore enhance the photocurrent production in photoactive materials for photoelectric devices, which is beneficial for photoelectric biosensing.

High photoelectric activity is a significant factor for the construction of a sensitive photoelectric biosensor; therefore, the corresponding photocurrent response of the AuNP/TNW/AuNP composite was examined first at an applied potential of 0 V in PBS (pH 7.4) with AM 1.5G simulated sunlight (Fig. 3b). All of the samples exhibited an increase in the photocurrent under illumination; however, no significant photocurrent changes were observed during the on–off cycles for the TNW sample because the TiO_2 was primarily stimulated by ultraviolet radiation, leading to low photocurrent generation. Compared to the pristine TNW sample, the photoanode after decorating with Au nanoparticles presents substantially higher photoactivity because of the enhanced photoabsorption and improved interfacial charge transfer induced from Au nanoparticles. A remarkable 14-fold enhancement in the photocurrent density was observed in the AuNP/TNW/AuNP (14.30 μA/cm^2) as compared with that of the pristine TNW (0.98 μA/cm^2). Noticeably, the AuNP/TNW/AuNP exhibited a 2-fold increase in photocurrent density compared to that of AuNP/TNW, which was without the aid of an Au underlayer (7.75 μA/cm^2). This result indicated the importance of the pre-deposited Au underlayers, which can act as a sink for charge carriers in influencing the photoelectric effect for the AuNP/TNW/AuNP composites where the photocurrent enhancement mainly arose from the promotion of interfacial charge-transfer induced by electron accumulation and Fermi level shift in Au underlayers because of the ability of Au to store and shuttle electrons (Abdulla-Al-Mamun et al., 2011; Chen et al., 2010). The mechanism of charge transfer for AuNP/TNW/AuNP composites on FTO is illustrated in Fig. 4. As the irradiation was absorbed by Au nanoparticles decorated on the TiO_2 surface, the effective SPR-induced electrons would transfer from the Au nanoparticles to the conduction band minimum of TiO_2, and subsequently transferred to Au underlayers, leading to accumulation of electrons in the Au underlayers. Such electron accumulation in the Au underlayer can boost the Fermi level of Au to more negative potentials closer to that of the FTO substrate, enabling an effective electron shuttle to the FTO, and finally promoting the efficiency of interfacial charge-transfer processes for the AuNP/TNW/AuNP composites. The above results demonstrated that the AuNP/TNW/AuNP composite had superior photoelectric activity for highly efficient photoelectric immune biosensing.

3.2. Analytical performances of the immunosensor for AFP detection

As a useful means to investigate the interfacial properties of the electrodes, electrochemical impedance spectra (EIS) for the AuNP/TNW/AuNP, Anti-AFP/AuNP/TNW/AuNP, and AFP/Anti-AFP/AuNP/TNW/AuNP electrodes were carried out in the 0.5 mM $[Fe(CN)_6]^{3-/4-}$ solution containing 0.1 M KCl, as shown in Fig. 5(a). A semicircle portion in high/medium frequency was observed in all Nyquist plots, which stands for the charge transfer resistance at the electrode interfaces and the electrode/electrolyte interfaces. As shown in Fig. 5(a) and Fig. S4, the AuNP/TNW/AuNP electrode has the smallest diameter in the high frequency area compared to TNW and AuNP/TNW electrodes, which suggests that it has the best electrical conductivity and highest charge transfer efficiency among all of the electrodes, illustrating that the decoration of Au nanoparticles and Au underlayer can greatly promote electron and charge transmission. These results were in agreement with the tendency of change in the photocurrent. After

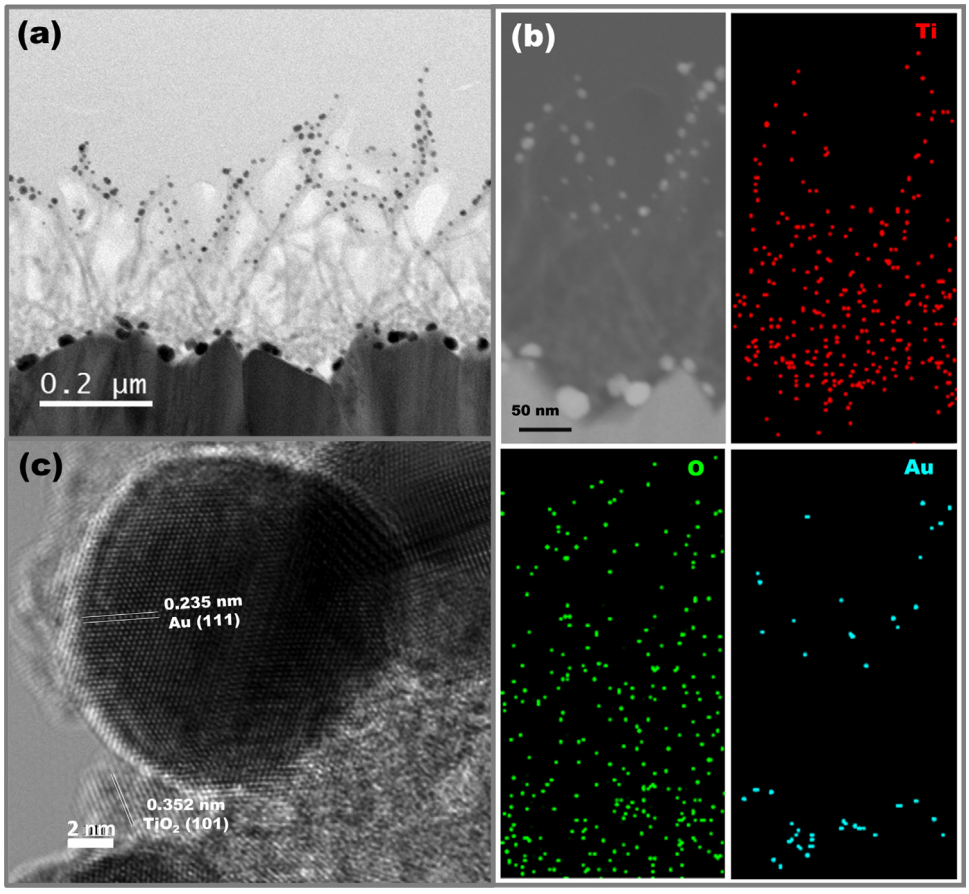

Fig. 2. Transmission electron microscopy (TEM) images of AuNP/TNW/AuNP composites. (a) Typical TEM image, (b) high-resolution TEM image, and (c) scanning transmission electron microscopy (STEM) image and corresponding elemental mappings of titanium, oxygen, and gold.

immobilization of the anti-AFP antibody on the AuNP/TNW/AuNP electrode (Anti-AFP/AuNP/TNW/AuNP), the diameter of the semi-circular curve was increased, which was due to the non-conductive effect from the anti-AFP antibody for obstructing the transfer of the electrons to the electrode, resulting in an increase in charge transfer resistance and also confirming the successful linkage of anti-AFP on the Au nanoparticle surface. After further binding of AFP, the resistance is further increased. The reason for the increase of the charge transfer resistance was the formation of an antibody-antigen immune complex, which gave rise to an additional barrier towards the $[Fe(CN)_6]^{3-/4-}$ redox probe and lead to an inhibition in charge transfer. The increased resistance would lead to change in the photocurrent. Their corresponding photocurrent response change is shown in Fig. 5(b), which characterizes the construction of the AuNP/TNW/AuNP electrical immunosensor for AFP. It was found that the photocurrent value for the AuNP/TNW/AuNP electrode would decrease after immobilizing the

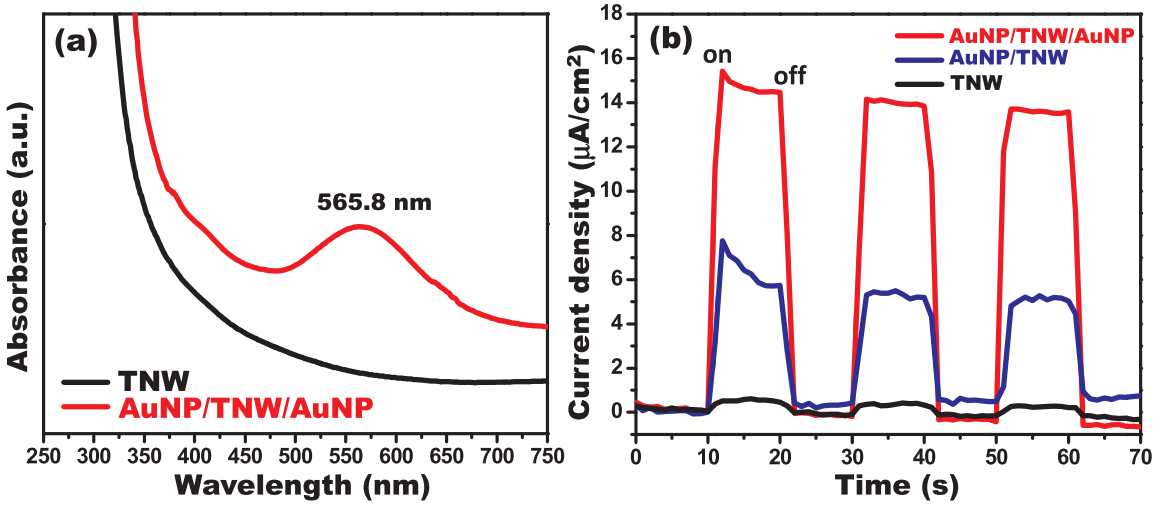

Fig. 3. (a) UV–vis absorption spectra of the TNW sample and sandwich-structured AuNP/TNW/AuNP composite. (b) Photocurrent response of TNW, AuNP/TNW (without the aid of an Au underlayer onto the surface of the FTO), and sandwich-structured AuNP/TNW/AuNP samples collected at 0 V versus Ag/AgCl in PBS solution at pH 7.4 with on–off cycles under AM 1.5G simulated sunlight.

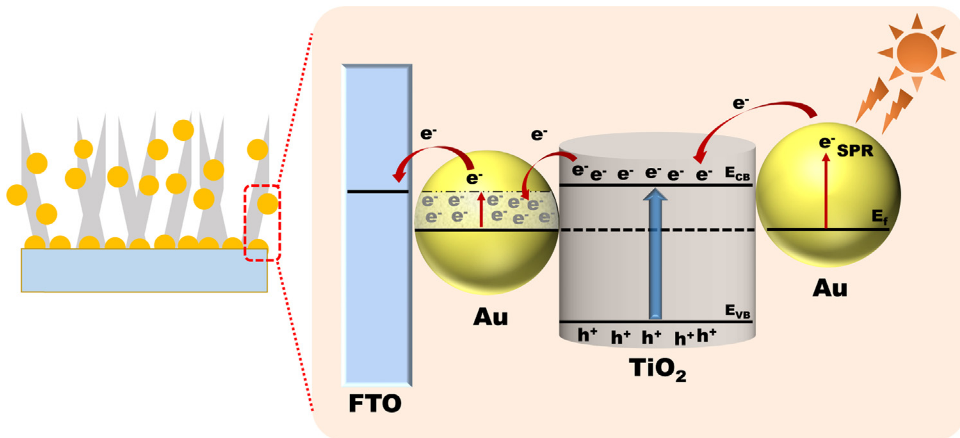

Fig. 4. The charge-transfer mechanism of the AuNP/TNW/AuNP composites on FTO. E_{CB}, conduction band; E_{VB}, valance band; E_f, Fermi energy level.

anti-AFP antibody, and then the photocurrent density was further reduced because of the specific recognition of AFP. The decrease of the photocurrent density could be ascribed to the immobilization of insulating biomolecules that would restrain the photoelectron transfer and reduce the photocurrent. The change of photocurrent intensity resulted from immobilization biomolecule could be applied for the quantitative analysis of AFP.

Given the change of the photocurrent response in the AuNP/TNW/AuNP immobilized electrodes as prospective market candidates for clinical practice, the label-free detection for the quantitative analysis of AFP protein was examined by monitoring the photocurrent change at an applied potential of 0 V under AM 1.5 G simulated sunlight. Fig. 6(a) depicts the calibration curve of the photocurrent change of AuNP/TNW/AuNP immunosensor after incubation with the AFP antigen at different concentrations in a PBS solution at pH 7.4. The concentration of AFP antigen has an important influence on the photocurrent responses, where the photocurrent decreased accordingly as the concentration of AFP increased. The variation of the photocurrent density has a linear relationship with the logarithm of the AFP concentration in a range from 0.001 to 10 ppb with a R-square of 0.99309 and a detection limit of 0.001 ppb (ng mL^{-1}) and S/N ratio of 3. It is noteworthy that the detection limit of the label-free sandwich-structured AuNP/TNW/AuNP photoelectric immunosensor for AFP detection without the use of any additional signal amplification treatment was comparable to the previously reported values of other AFP antigen sensing systems, such as 0.02 ng mL^{-1} for CdS-modified mesoporous TiO_2 film (Yang et al., 2015b), 40 pg mL^{-1} for the TiO_2/CdS hybrid (Wang et al., 2009), 0.2 pg mL^{-1} for the g-C_3N_4 modified electrodes with CA as the electron donor (Yuan et al., 2016), 8 pg mL^{-1} for Ag_2S nanoparticles modified with a macroporous ZnO inverse opals structure (Jiang et al., 2016), 0.13 pg mL^{-1} for TiO_2 coupled with AFP–CdTe–GOx bioconjugates (Li et al., 2012), 0.01 ng mL^{-1} for ZnO inverse opal electrodes with signal amplification of CdS-QDs (Xu et al., 2015), and 0.56 pg mL^{-1} for Au-ZnO flower-rod heterostructures (Han et al., 2017). The enhanced detection ability of the AuNP/TNW/AuNP photoelectric immunosensor suggests that the introduction of Au nanoparticles and the building of the porous frameworks can efficiently improve the photoelectric effect of the electrode because of the improved light harvesting and enhanced charge separation from Au particles as well as the reduced incident light reflection from the porous frameworks. Therefore, the abovementioned results demonstrated that the proposed AuNP/TNW/AuNP photoelectric immunosensor has been fabricated successfully and can be used to effectively detect AFP.

In addition to the established sensitivity, selectivity is also an important factor for successfully developing biosensor chips for clinical diagnosis. To demonstrate that the enhanced AFP detection was specific, the response of 10 ppm IgG and 10 ppm HBV protein on this sensor was compared to that of the AFP antigen at 0.001 ppb, as illustrated in Fig. 6(b). No significant change in photocurrent response was observed to the additions of IgG and HBV protein to the immunosensor,

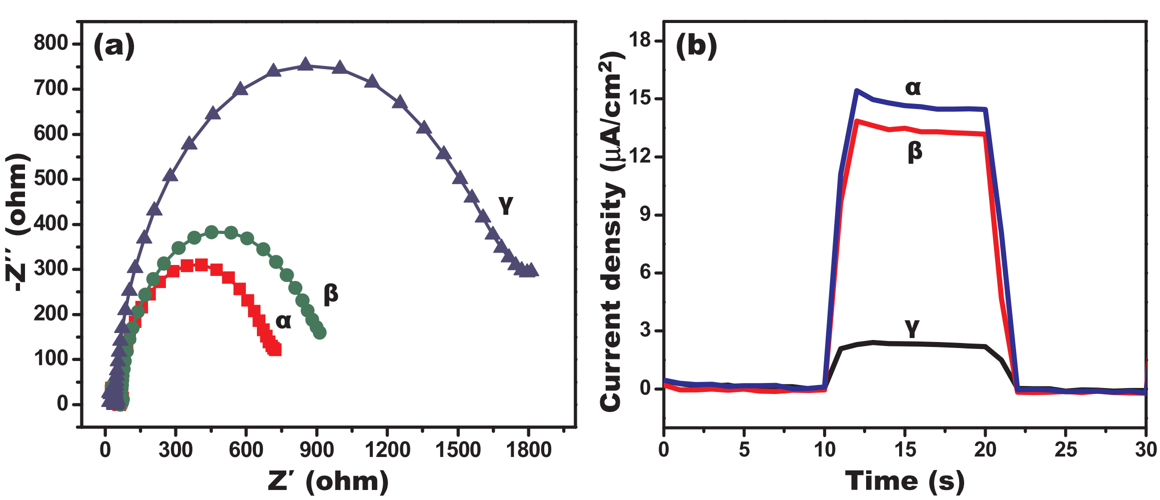

Fig. 5. EIS Nyquist plot in the 0.5 mM $[Fe(CN)_6]^{3-/4-}$ solution containing 0.1 M KCl with a frequency range between 0.01 and 100 kHz (a) and photocurrent response in PBS at pH 7.4 (b) under AM 1.5G simulated sunlight of (α) AuNP/TNW/AuNP composite electrode, (β) Anti-AFP/AuNP/TNW/AuNP, and (γ) AFP/Anti-AFP/AuNP/TNW/AuNP.

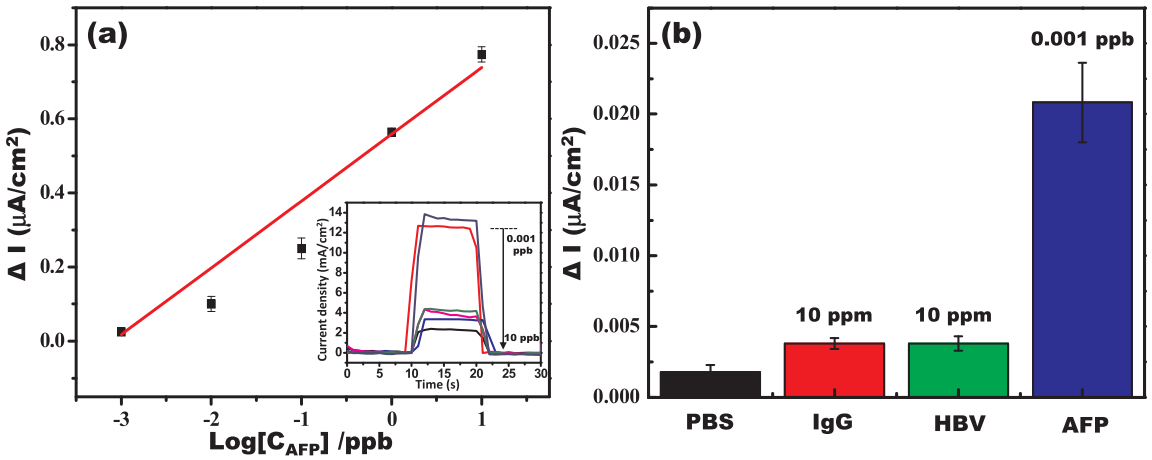

Fig. 6. Calibration curve corresponding to the analysis of different AFP concentrations of 0.001, 0.01, 0.1, 1, and 10 ppb. ΔI is the difference between I_0 and I, where I_0 is the photocurrent density of the anti-AFP/AuNP/TNW/AuNP, and I is the AFP/Anti-AFP/AuNP/TNW/AuNP under different concentration. (b) Selectivity towards a different analyst.

while a remarkable photocurrent enhancement in the presence of the AFP antigen in the same experimental conditions can be obtained according to specific antigen–antibody binding. Hence, these results indicated that the specificity of the prepared label- and amplification-free AuNP/TNW/AuNP photoelectric immunosensor was satisfactory.

3.3. Practical determination of AFP in human serum

In order to evaluate the practicability of the prepared sandwich-structured AuNP/TNW/AuNP photoelectric immunosensors for practical clinical analysis, the detection of AFP in human serum by using the proposed photoelectric sensors and the commercialized available ELISA method were conducted. As shown in Table S1, the recoveries were between ~98% and ~116% and the relative standard deviation (RSD) were from ~2% and ~4%, as measured by proposed photoelectric sensors. In addition, it should be noted that the calculated concentrations revealed a good agreement with the values obtained from the commercial ELISA method with the relative errors in the range from ~− 9% to ~4%. These results demonstrated that the designed AuNP/TNW/AuNP photoelectric immunosensors could meet the demand for clinical detection of AFP in practical serum samples.

4. Conclusion

In summary, we have developed a label- and amplification-free and ultrasensitive SPR-enhanced photoelectric sensor based on a unique layer-by-layer sandwich-structured AuNP/TNW/AuNP composite on FTO for the detection of biomarker AFP. The Au nanoparticle can provide a strong LSPR effect and effective interfacial charge transfer as well as improved light harvesting, resulting in a high increment of photocurrent density, which was beneficial for biomolecular sensitive detection. The proposed immunosensor of AuNP/TNW/AuNP coupled with anti-AFP showed high sensitivity and good specificity to its antigen of AFP, with an excellent detection limit of 0.001 ppb (ng mL^{-1}), which is the lowest detection limit for the AFP antigen that has been reported. Furthermore, detection of AFP in human serum samples was performed. These results indicated that proposed photoelectric immunosensor exhibited high sensitivity and specificity, offering a promising opportunity for AFP detection in clinical diagnostics. Moreover, this strategy could provide a promising sensing strategy designed for the detection of other biomolecules in clinical diagnosis with satisfactory results through a simple equipment and convenient operation.

Acknowledgment

We gratefully acknowledge the financial support from Ministry of Science and Technology, Taiwan (104-2113-M-005-011-MY3; 106-2627-M-005-001-; 107-2113-M-005-008-; 107-2627-M-005-001-). We also thank Dr. Yin-Cheng Yen at National Tsing Hua University, Taiwan, for providing technical assistance in optimization of the AuNP/TNW/AuNP synthesis.

Appendix A. Supporting information

Supplementary data associated with this article can be found in the online version at doi:10.1016/j.bios.2018.11.020.

References

Abdulla-Al-Mamun, M., Kusumoto, Y., Zannat, T., Islam, M.S., 2011. Phys. Chem. Chem. Phys. 13, 21026–21034.
An, Y.R., Tang, L.L., Jiang, X.L., Chen, H., Yang, M.C., Jin, L.T., Zhang, S.P., Wang, C.G., Zhang, W., 2010. Chem.-Eur. J. 16, 14439–14446.
Atwater, H.A., Polman, A., 2010. Nat. Mater. 9, 205.
Bai, J., Zhou, B., 2014. Chem. Rev. 114, 10131–10176.
Bora, T., Zoepfl, D., Dutta, J., 2016. Sci. Rep. 6, 26913.
Chen, J.-Z., Ko, W.-Y., Yen, Y.-C., Chen, P.-H., Lin, K.-J., 2012. ACS Nano 6, 6633–6639.
Chen, J., Gao, P., Wang, H., Han, L., Zhang, Y., Wang, P., Jia, N., 2018a. J. Mater. Chem. C. 6, 3937–3944.
Chen, Y., Li, Y., Deng, D., He, H., Yan, X., Wang, Z., Fan, C., Luo, L., 2018b. Biosens. Bioelectron. 102, 301–306.
Chen, J., Luo, J., Jin, X., Liu, Y., Sun, J., Gao, L., 2013. Electrochim. Acta 100, 85–92.
Chen, W.-H., Ko, W.-Y., Chen, Y.-S., Cheng, C.-Y., Chan, C.-M., Lin, K.-J., 2010. Langmuir 26, 2191–2195.
Devadoss, A., Sudhagar, P., Terashima, C., Nakata, K., Fujishima, A., 2015. J. Photochem. Photobiol. C: Photochem. Rev. 24, 43–63.
Dong, W., Zhang, T., Epstein, J., Cooney, L., Wang, H., Li, Y., Jiang, Y.-B., Cogbill, A., Varadan, V., Tian, Z.R., 2007. Chem. Mater. 19, 4454–4459.
Feng, J., Li, Y., Gao, Z., Lv, H., Zhang, X., Fan, D., Wei, Q., 2018. Biosens. Bioelectron. 99, 14–20.
Gao, P., Ma, H., Yang, J., Wu, D., Zhang, Y., Du, B., Fan, D., Wei, Q., 2015. New J. Chem. 39, 1483–1487.
Guo, L., Li, Z., Marcus, K., Navarro, S., Liang, K., Zhou, L., Mani, P.D., Florczyk, S.J., Coffey, K.R., Orlovskaya, N., et al., 2017a. ACS Sens. 2, 621–625.
Guo, Q., Liu, L., Zhang, M., Hou, H., Song, Y., Wang, H., Zhong, B., Wang, L., 2017b. Biosens. Bioelectron. 92, 654–660.
Haddour, N., Chauvin, J., Gondran, C., Cosnier, S., 2006. J. Am. Chem. Soc. 128, 9693–9698.
Han, Q., Wang, K., Xu, L., Yan, X., Zhang, K., Chen, X., Wang, Q., Zhang, L., Pei, R., 2015. Analyst 140, 4143–4147.
Han, Z., Luo, M., Chen, L., Chen, J., Li, C., 2017. Appl. Surf. Sci. 402, 429–435.
Hsu, C.-Y., Huang, J.-W., Lin, K.-J., 2011. Chem. Commun. 47, 872–874.
Jazayeri, M.H., Amani, H., Pourfatollah, A.A., Pazoki-Toroudi, H., Sedighimoghaddam, B., 2016. Sens. Bio-Sens. Res. 9, 17–22.
Jiang, Y., Liu, D., Yang, Y., Xu, R., Zhang, T., Sheng, K., Song, H., 2016. Sci. Rep. 6, 38400.

Li, R., Yan, R., Bao, J., Tu, W., Dai, Z., 2016. Chem. Commun. 52, 11799–11802.
Li, Y.-J., Ma, M.-J., Zhu, J.-J., 2012. Anal. Chem. 84, 10492–10499.
Liu, X.-P., Chen, J.-S., Mao, C.-j., Niu, H.-L., Song, J.-M., Jin, B.-K., 2018. Biosens. Bioelectron. 116, 23–29.
Lu, W., Wang, G., Jin, Y., Yao, X., Hu, J., Li, J., 2006. Appl. Phys. Lett. 89, 263902.
Pu, Y.-C., Wang, G., Chang, K.-D., Ling, Y., Lin, Y.-K., Fitzmorris, B.C., Liu, C.-M., Lu, X., Tong, Y., Zhang, J.Z., et al., 2013. Nano Lett. 13, 3817–3823.
Tang, J., Kong, B., Wang, Y., Xu, M., Wang, Y., Wu, H., Zheng, G., 2013. Nano Lett. 13, 5350–5354.
Wang, G.-L., Xu, J.-J., Chen, H.-Y., Fu, S.-Z., 2009. Biosens. Bioelectron. 25, 791–796.
Wang, H., Wang, Y., Zhang, Y., Wang, Q., Ren, X., Wu, D., Wei, Q., 2016. Sci. Rep. 6, 27385.
Wang, P., Dai, W., Ge, L., Yan, M., Ge, S., Yu, J., 2013. Analyst 138, 939–945.
Wang, Y., Bai, L., Wang, Y., Qin, D., Shan, D., Lu, X., 2018. Analyst 143, 1699–1704.
Xu, R., Jiang, Y., Xia, L., Zhang, T., Xu, L., Zhang, S., Liu, D., Song, H., 2015. Biosens. Bioelectron. 74, 411–417.
Yang, J.J., Gao, P.C., Liu, Y.X., Li, R.X., Ma, H.M., Du, B., Wei, Q., 2015a. Biosens. Bioelectron. 64, 13–18.
Yang, X., Li, J., Fu, J., 2015b. Anal. Methods 7, 1328–1332.
Yen, Y.-C., Chen, J.-A., Ou, S., Chen, Y.-S., Lin, K.-J., 2017. Sci. Rep. 7, 42524.
Yen, Y.-C., Chen, P.-H., Chen, J.-Z., Chen, J.-A., Lin, K.-J., 2015. ACS Appl. Mater. Interfaces 7, 1892–1898.
Yu, Y., Wen, W., Qian, X.-Y., Liu, J.-B., Wu, J.-M., 2017. Sci. Rep. 7, 41253.
Yuan, F., Gu, T.-T., Li, X.-Q., Wang, G.-L., 2016. J. Electroanal. Chem. 783, 226–232.
Zhang, G., Zhao, Z., Tan, H., Zhao, H., Qu, D., Zheng, M., Yu, W., Sun, Z., 2015. RSC Adv. 5, 21237–21241.
Zhang, Y., Shoaib, A., Li, J., Ji, M., Liu, J., Xu, M., Tong, B., Zhang, J., Wei, Q., 2016. Biosens. Bioelectron. 79, 866–873.
Zhang, Z., Zhang, L., Hedhili, M.N., Zhang, H., Wang, P., 2013. Nano Lett. 13, 14–20.
Zhao, Z., Zhu, X., Zuo, M., Xu, J., Wang, Y., 2016. CrystEngComm 18, 1636–1644.